Acta Astronautica 210 (2023) 82–94

Contents lists available at ScienceDirect

Acta Astronautica

journal homepage: www.elsevier.com/locate/actaastro

Research paper

Nuclear fusion powered Titan aircraft

Michael Paluszek [a,*], Annie Price [a,1], Zoe Koniaris [a,2], Christopher Galea [a], Stephanie Thomas [a], Samuel Cohen [b], Rachel Stutz [a,3]

[a] Princeton Satellite Systems, 6 Market St. Suite 926, Plainsboro, NJ, USA
[b] Princeton Plasma Physics Laboratory, 100 Stellarator Rd, Princeton, NJ, USA

ARTICLE INFO

Keywords:
Fusion propulsion
Titan
Aircraft
Nuclear propulsion
Mars
Space power

ABSTRACT

This paper discusses a system for Titan exploration enabled by nuclear fusion power. Titan is one of the most interesting locations in the solar system with a thick atmosphere, surface oceans, under-ice oceans and complex terrain. This paper provides a conceptual design of a fusion-powered system to explore many parts of Titan and enable the use of high-power instruments. The design includes a fusion-powered orbital transfer vehicle and an electric Titan science aircraft. A Direct Fusion Drive (DFD) propulsive engine could bring a sizable spacecraft to Titan orbit in less than two years. A second fusion reactor, configured as a closed-loop power generator, would be used for an electric Titan science aircraft. Both reactors are based on the Princeton Field-Reversed Configuration (PFRC) concept which combines an FRC with a magnetic mirror. PFRC uses a novel radio-frequency plasma heating system and deuterium-helium-3 fuel. A lower temperature plasma flows around the closed-field FRC region removing the fusion products. In the DFD propulsive configuration, this secondary flow permits direct and variable thrust and exhaust velocity. The science aircraft would do a powered entry to Titan and then have the capability to fly anywhere on the moon at subsonic speeds. The DFD-powered transfer vehicle would allow the in-orbit transfer stage to change inclination as needed to cover different areas of the surface.

1. Introduction

Recent work by Gajeri, Aime, and Kezerashvili [1], demonstrated that a spacecraft powered by Direct Fusion Drive could reach Titan in less than 2.6 years with a 2 MW power plant for a payload mass of 1000 kg. This paper extends that work to include as a payload a Titan aircraft that can enter the atmosphere and fly around Titan for years. The fusion-powered electric aircraft is propelled by ducted fans. Entry does not use any thrust. The fusion-propelled transfer vehicle stays in orbit with its scientific payloads and acts as a communications node for the Titan aircraft. The Titan aircraft would have over 100 kWe for Titan science, several orders of magnitude greater than will be available to Dragonfly. [2].

2. Titan mission

2.1. The Titan environment

A composite infrared image of Titan from the NASA Cassini mission is shown in Fig. 1. The complexity of the geography is evident.

The surface of Titan [3] is obscured by a hazy atmosphere. It has standing bodies of liquid, including rivers, lakes, and seas. Titan may have volcanos with liquid water lava. Extensive regions of dunes stretch across Titan in the equatorial areas.

Titan does not have its own magnetic field, but it does orbit within the magnetosphere of Saturn [4]. Its thick atmosphere protects the surface from ionizing radiation.

2.2. Dragonfly science objectives

Dragonfly's primary goal is [5] to study Titan prebiotic chemistry and to look for chemical bio-signatures of water-based life. The quadcopter is shown in Fig. 2.

Dragonfly's target is the 80 km diameter Selk Crater shown in Fig. 3. Its location on Titan is shown in Fig. 4.

Dragonfly's major instruments are shown in Table 1. The entire spacecraft is about 450 kg and the power produced by the MMRTG is about 70 W. [6].

* Corresponding author.
E-mail address: map@psatellite.com (M. Paluszek).
[1] Current affiliation: Air Force Institute of Technology, Wright-Patterson AFB, OH, USA.
[2] Current affiliation: Princeton University, Princeton, NJ, USA.
[3] Current affiliation: Stanford University, Stanford, CA, USA.

https://doi.org/10.1016/j.actaastro.2023.04.029
Received 29 December 2022; Received in revised form 7 April 2023; Accepted 15 April 2023
Available online 25 April 2023

Table 1
Dragonfly science payload.

Name	Description
Dragonfly mass spectrometer	A linear ion trap mass spectrometer
Dragonfly gamma-ray and neutron spectrometer	Measure bulk elemental composition in the shallow subsurface
Dragonfly geophysics and meteorology package	Measure atmospheric temperature, pressure, wind speed and direction, methane humidity, hydrogen partial pressure, crustal seismicity, electric field, surface dielectric properties, surface temperature, and ambient sound
Dragonfly camera suite	Dragonfly carries eight scientific cameras

Acronyms

FRC	Field Reversed Configuration
JIMO	Jupiter Icy Moon Orbiter
DFD	Direct Fusion Drive
MeV	Million electron volts 6×10^{-14} J
MMRTG	Multi-Mission Radioisotope Generator
NIAC	NASA Innovative Advanced Concepts
PFRC	Princeton Field-Reversed Configuration
PSS	Princeton Satellite Systems
RF	Radio Frequency
RMF	Rotating Magnetic Field

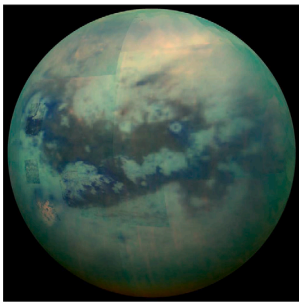

Fig. 1. Titan composite infrared image of Titan courtesy of NASA. This shows the complexity of the moon and the need for global coverage.

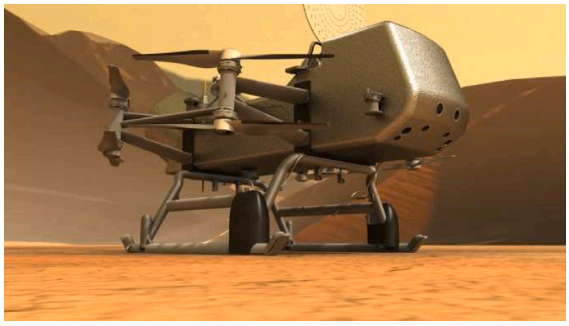

Fig. 2. The Dragonfly quadcopter. Image courtesy of NASA. Due to its limited power and size, it can only study a small area on Titan.

2.3. Science objectives

This mission expands on the Dragonfly mission and incorporates elements of previously proposed Titan missions. Dragonfly aims to study Titan's atmosphere, surface, and subsurface ocean by sampling various sites around the moon, and it is one of the first NASA missions since the Viking landers to explicitly include a search for signs of life [5]. This mission would continue that search with the Titan Aircraft. In particular, the Titan Aircraft will greatly expand the area of Titan's surface that could be studied in depth. The Huygens probe was only able to transmit a few hours' worth of data about Titan's atmosphere, including only one point on the surface of the moon [7]. The Dragonfly quadcopter will be able to move on Titan's surface, but its mobility will still be limited by its power and speed. The Titan Aircraft would have a longer and more extensive mission due to fusion-enabled speed and power. This would make it ideal for using imaging or radar techniques to map out an unprecedented amount of Titan's surface.

The mission could also support additional science payloads. A submarine to explore Titan's oceans more in-depth has received a Phase II NIAC grant [8], and NASA/ESA's proposed Titan Saturn System Mission (TSSM) included a Montgolfière balloon intended to circumnavigate Titan and image its surface [9]. Payloads similar to either or both of these proposed instruments could be included in this mission, possibly being deployed from the Titan Aircraft. The Titan submarine has a maximum power requirement of 842 W and a mass of 100 kg while the balloon has a power requirement of 1.8 kW and mass of 25 kg, both of which are only fractions of the available power (500 kW) and mass (1000 kg) available for science missions on the Titan Aircraft. Experiments such as these or others intending to image or sample Titan's surface would bring a new depth of knowledge about Titan's properties and potential to harbor life.

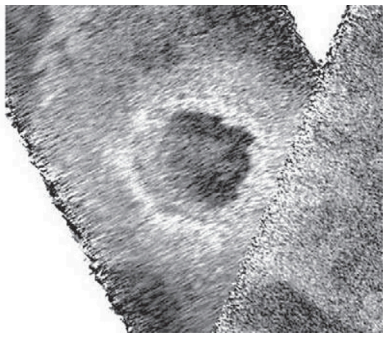

Fig. 3. The Selk crater. Image courtesy of NASA. This is Dragonfly's area of study.

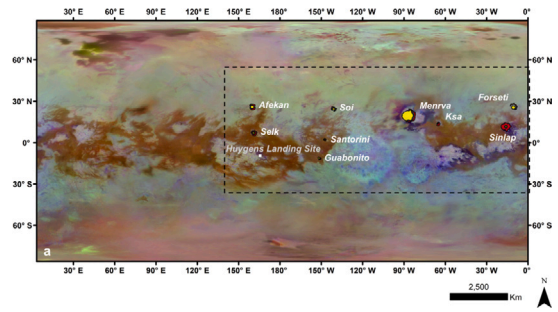

Fig. 4. The location of the Selk crater on Titan. Selk is in the middle. Image courtesy of NASA.

Table 2
RF sounder power requirements.

Science objectives	Power (W)
Subsurface sounding	10000
Magnetospheric sounding	10–10000
Ionospheric sounding	100–500
Local resonances	10000

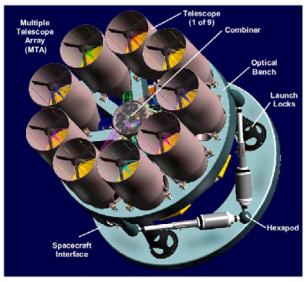

Fig. 5. MIDAS sensor [16].

The science goals of this mission would follow those set out in the TSSM report [9]:

- *Titan: an Earthlike System.* How does Titan function as a system; to what extent are there similarities and differences with Earth and other solar system bodies?
- *Titan's Organic Inventory.* To what level of complexity has prebiotic chemistry evolved in the Titan system?

2.4. High power instruments

The NASA Jupiter Icy Moon Orbiter mission (JIMO) had a 100 kWe nuclear fission reactor for power and propulsion. Instruments were proposed that could take advantage of that power level. An advanced radio sounder instrument was proposed that could be used on a wide variety of outer planet missions [10]. This instrument would provide diverse measurements necessary for detection of subsurface oceans and for characterization of moon ionospheres, magnetosphere-moon interactions, and permanent or induced magnetic fields. Different frequency ranges were proposed for different applications. Table 2 gives the power requirements.

A National Research Council (NRC) study [11] lists a large number of missions enabled by nuclear power systems. The need for nuclear power is mostly for propulsion. Instruments relevant to a Titan mission include radar, specifically high-power, ground-penetrating, and synthetic-aperture radar systems, and laser-ablation spectrometers. JIMO also planned to use 1000 W for its communication system [12]. JIMO allocated 45 kWe to the science payload [13]. Hartman lists 250 kWe as a future goal for a nuclear powered spacecraft. Table 3 lists the JIMO instruments. Four require power greater than 1 kWe. All four would be potential Titan instruments. Hart [14] gives a peak power demand of 25269 W.

The Multiple Instrument Distributed Aperture Sensor (MIDAS) for remote sensing [16] is an example of an instrument enabled by the availability of high power. In its active remote sensing modes using an integrated laser source, MIDAS, shown in Fig. 5 enables LIDAR, vibrometry, illumination, various active laser spectroscopies such as ablative, breakdown or time-resolved spectroscopy. The MIDAS optical design also provides high-resolution imaging for long dwell times at high altitudes, thereby enabling real-time, wide-area remote sensing of dynamic changes in planet surface processes.

Another is the high-capability Planetary Advanced Radio Sounder (PARS) [17]. This high-power, high-data rate remote-sensing instrument will provide critical and diverse measurements necessary for detection of subsurface oceans and for characterization of ionospheres of moons, magnetosphere-moon interactions, and permanent or induced magnetic fields for missions to icy moons and other bodies in the solar system. This information is critical to determining if life is possible on moons of this type.

2.5. Mission economics

Table 4 gives the economics for several scientific missions. A simple metric is dollars per watt for the science mission. Power needs to be divided between experiments and data transmission. All else being equal, the data rate is proportional to power. The power available to transmission determines the science that can be returned. Of course, careful use of bandwidth maximizes the return for a given power level. The Jupiter Icy Moon Orbiter (JIMO) which would have used a nuclear reactor is seen as a real bargain. Transfer time is another measure as it is the delay in scientific return, essentially the investment in the mission does not produce a return on investment until after the transfer. The operations cost is also proportional to the duration. Operations costs range from $15M/year for New Horizons to $50M/year for other spacecraft.

3. Mission plan

The mission plan is

1. Launch on a heavy lift launcher such as SLS, Falcon 9 Heavy, or the Delta Heavy
2. Direction insertion into a heliocentric orbit
3. Constant acceleration to Saturn
4. Entry into Saturn orbit
5. Rendezvous with Titan
6. Entry into Titan Orbit
7. Separation of the aircraft; transfer vehicle remains in orbit
8. Unpowered aerodynamic entry of aircraft into the Titan atmosphere
9. Separation of the ducted fan shrouds
10. Fly to the first landing zone
11. Powered landing on Titan

The transfer to Titan is covered in [1]. The aircraft will conduct experiments in the landing area. It will then fly to other locations. The orbiter will provide full surface reconnaissance and can provide maps of the surface to the aircraft. The aircraft will build maps of the surface as it flies around the moon. With time, it will be able to identify Titan's unique features. The velocity changes for the mission from Earth are shown in Table 5.

The power and payload mass for each vehicle, the transfer vehicle and the aircraft payload, are summarized in Table 6 and described further in later sections. The payload for the orbital transfer vehicles includes the aircraft and the orbital bus and instruments. The payload for the aircraft is its dry mass.

4. Fusion power plant

The Princeton Field-Reversed Configuration (PFRC) and Direct Fusion Drive have been previously presented at the IAC conferences in 2012 [18,19], 2014 [20], and 2015 [21]. Initial mission analysis had been performed under Princeton Satellite Systems (PSS) internal research & development funds, while work on the PFRC experiment was funded at the Princeton Plasma Physics Lab (PPPL) by the Department of Energy. PSS has now received three research contracts from NASA and one from ARPA-E to further develop the DFD concept. Prior papers [22–24] describe some of the underlying physics. A review paper on the PFRC reactor concept has recently been published [25] which includes the status of development, the proposed path toward a reactor, and the commercialization potential of a PFRC reactor. We will provide a summary here for the reader's convenience.

Table 3
JIMO instruments [14,15].

Instrument	Mass (kg)	Average power (W)	Peak power (W)	Location
Super high-res camera	65	100	100	Scan platform
High res telescope	20	5	5	Scan platform
Mapping camera	5	5	5	Scan platform
Wide-angle camera	3	5	5	Scan platform
Hyperspectral imager	25	15	15	Scan platform
Thermal imager	11	14	14	Scan platform
SAR topographic mapper	150	200	1400	Bus-mounted (on boom)
Interferometric SAR		1683	7923	
Ice penetrating radar	50	2700	13000	Bus-mounted
Laser-illumination spectrometer	250	2500	2500	Bus-mounted
Laser altimeter	44	1400	1400	Bus-mounted
Plasma wave spectrometer	10	7	7	Bus-mounted
Magnetometer	3	3	3	Bus-mounted (on boom)
Ion and neutral mass spectrometer	10	28	28	Turntable
Heavy ion counter	3.3	7	7	Turntable
Energetic particle detector	11	10	10	Turntable
Plasma spectrometer	13	11	11	Turntable
Dust detector	5	6	6	Turntable
Auxiliary science package		375		Bus-mounted

Table 4
Mission capability cost is $/Watt.

Mission	Cost ($B)	Power (W)	Transfer (Years)	$/W
JIMO	16	100,000	5	160,000
New Horizons	0.78	202	9	3,861,386
Juno	0.7	435	5	1,609,195
BepiColumbo	0.7735	420	7	1,841,666
Dragonfly	1	70	9	14,285,714

Table 5
Velocity changes using the continuous thrust plan from [1].

Mission phase	Δv (km/s)
Earth departure	7.56
Interplanetary acceleration	14.50
Interplanetary deceleration	36.03
Saturn orbit insertion	18.90
Titan orbit insertion	1.57
Total	78.57

Table 6
Vehicle power and payloads.

Vehicle	Transfer vehicle	Titan aircraft
Fusion power	2.4 MW	1.15 MW
Thrust power	1.4 MW	N/A
Electrical power	0.1 MW	0.5 MW
Reactor mass	2531 kg	1006 kg
Payload mass	3500 kg	2000 kg

4.1. DFD summary

The PFRC employs a radio frequency (RF) plasma heating method, odd-parity rotating magnetic field (RMF) heating, first theorized in 2000 [22] and demonstrated in the PFRC-1 experiment in 2006 [23]. Experiments are ongoing with the second-generation machine, PFRC-2, (Fig. 6). Results from experimental studies of electron heating in PFRC-2 have surpassed theoretical predictions, with minority electron populations reaching 500 eV and pulse lengths of 300 ms. Experiments to measure ion heating with input power up to 200 kW are ongoing. When scaled up to achieve fusion parameters, PFRC would result in a 4–8 m long, 1.5 m diameter reactor producing 1 to 10 MW. This reactor would be uniquely small and clean among all fusion reactor concepts, producing very low levels of neutrons. Neutrons would be at 2.45 MeV, much lower energy than D-T reaction neutrons, and would only be produced by D-D side reactions. Neutrons cannot be directed and therefore do not contribute to thrust.

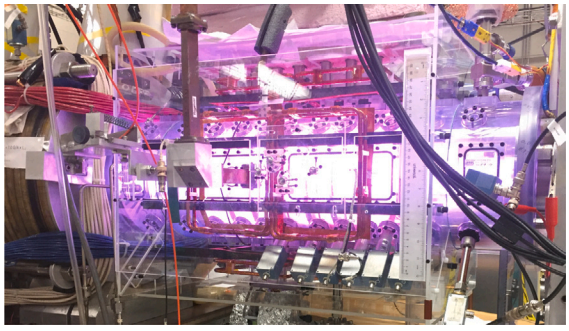

Fig. 6. A plasma shot in the PFRC-2 experiment at PPPL.

A component diagram of the engine is shown in Fig. 7. The startup system, for energizing the superconducting coils, spinning up the Brayton cycle compressor, and starting the fusion reaction, is in the upper right corner [26]. The fusion vacuum vessel is orange. The RMF system is depicted above the vacuum vessel. Coil refrigeration is on the right. The heat recycling system is on the bottom.

Attempts have been made to heat FRC plasmas with RF before, but generally with a picture-frame antenna that resulted in a near-FRC plasma but with open magnetic field lines. We call this even-parity heating due to the symmetry of the induced magnetic field. Open field lines allow the plasma to escape and reduce confinement time. In contrast, each of the four PFRC antenna sections is two joined rectangles. Two pairs operate 90° out of phase on adjacent sides of the plasma. An antenna (wrapped in orange Kapton tape) is visible on the side of PFRC-2 in Fig. 6. This results in so-called odd-parity heating – the magnetic field on one side of each figure-8 is in the opposite direction as the other side – and closed field lines in the generated FRC. Closed field lines keep the plasma trapped as it is heated. The oscillation of the currents in the RF antenna results in a rotating magnetic field, with about 0.1%–1% of the strength of the axial magnetic field.

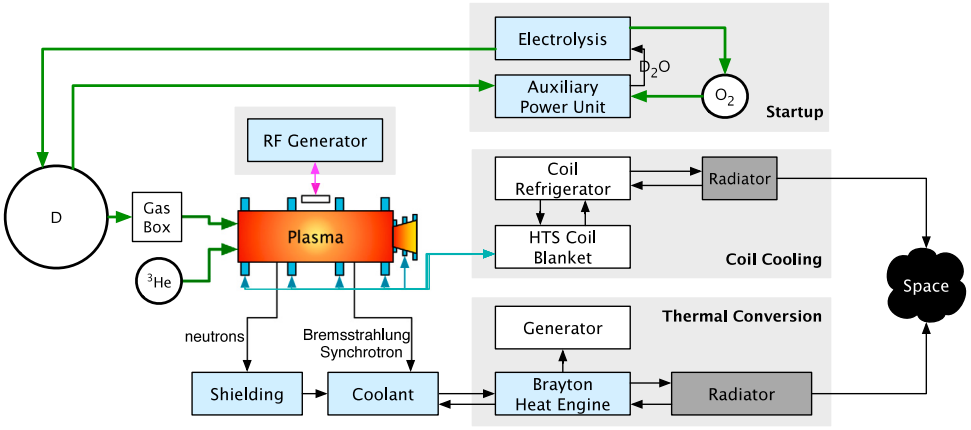

Fig. 7. Block diagram of the DFD engine.

The PFRC is specifically designed to have ultra-low radioactivity. Being a "high-β" machine, that maintains a high ratio of the plasma pressure to magnetic pressure (β), the PFRC should achieve the high temperatures necessary to burn helium-3 (^{3}He) and deuterium (D) in a compact machine. The reaction equations are:

$$D + {}^3He \rightarrow {}^4He\ (3.6\ MeV) + p\ (14.7\ MeV) \quad (1)$$

$$D + D \rightarrow T\ (1.01\ MeV) + H\ (3.02\ MeV) \quad (2)$$

$$D + D \rightarrow {}^3He\ (0.82\ MeV) + n\ (2.45\ MeV) \quad (3)$$

$$D + T \rightarrow {}^4He\ (3.5\ MeV) + n\ (14.1\ MeV) \quad (4)$$

Simply burning ^{3}He-D at high temperatures in a large FRC reactor could result in an increase in neutrons due to the above D-D and D-T side reactions. PFRC has three features that greatly reduce the number and impact of the neutrons from this baseline: one, the small size of the reactor (~25 cm plasma radius) results in a favorable ratio of surface area to plasma volume, reducing the wall load compared to larger machines; two, the operating fuel ratio of ^{3}He:D could be adjusted upwards to as much as 3:1, sacrificing some power density for lower neutron production; three, the reactor is designed to rapidly eliminate the tritium (T) produced by the D-D side reactions, preventing any D-T reactions from occurring. This means that the only neutrons produced are those with an energy of 2.45 MeV.

The tritium is eliminated due to its interaction with the shell plasma surrounding the fusion region. The size of the reactor is such that the so-called FRC s-parameter, [27] which scales with the ratio of the fusion-product triton gyro-radius to the scrape-off-layer radius, is low — about 2.3. This forces the tritons to pass through the shell plasma repeatedly. When the tritons pass through the cool shell plasma, electron drag causes energy to be transferred from the tritons to the shell plasma electrons. The triton is quickly captured by the shell plasma field lines and flows out the open end of the reactor. The burn-up time for energetic tritons to fuse is about 20 s, while the time in which it will cool and be trapped in the shell plasma is less than 0.01 s [21,28]. The same process occurs for the other fusion ash products, which are all effectively exhausted.

The PFRC is well suited for use as space propulsion for two reasons: one, the configuration and small size results in a tremendous reduction of neutron production compared to other D-^{3}He approaches, as described above; two, the directed axial flow of cool shell plasma which absorbs the energy of the fusion products. When the divertor end of the PFRC is configured with a magnetic nozzle, the reactor becomes the Direct Fusion Drive (DFD). Adding additional propellant to the external flow results in a moderate thrust, and high specific impulse exhaust stream. This process is called *thrust augmentation*. The low neutron production is crucial to minimizing the shielding required while in transit, maximizing the engine-specific power. The maximum

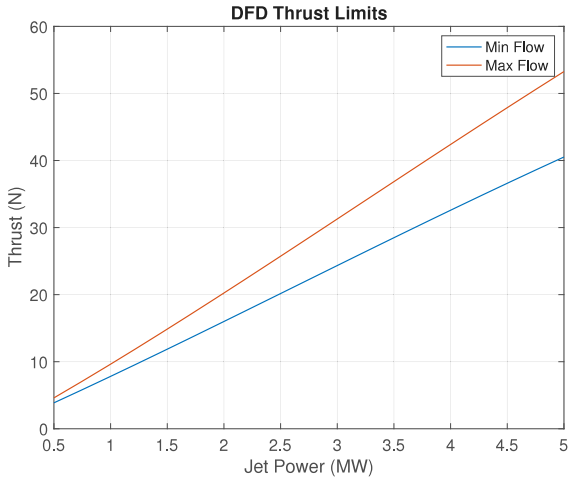

Fig. 8. Maximum DFD thrust as a function of jet power.

thrust for a given power, based on UEDGE [29] is given in Fig. 8. This leads to a practical lower exhaust velocity limit of 70 km/s assuming a 0.4 power to thrust conversion efficiency.

There are several factors which could allow PFRCs to be smaller than other magnetic confinement fusion devices, which are discussed in Ref. [25]. These include: (1) FRCs with zero toroidal magnetic field (only a poloidal field is present), resulting in a safety factor q of 0, have substantially decreased neoclassical transport losses which scale as $(1 + q^2)$ compared with, e.g., tokamaks, which have $q > 3$, so that FRCs should have 10 times better energy confinement given the same magnetic field and plasma temperature. (2) Turbulence-enhanced transport would be mitigated in a PFRC-type reactor due to the larger scale of thermal ion orbits in the machine compared to turbulence length scales — only when ion gyro-orbits are much smaller than the turbulence length scales, such as in tokamaks, does enhancement of turbulence become substantial. (3) Thermal diffusivity would decrease by 3x due to the 10x increase in temperature of a PFRC-type reactor compared to a D-T tokamak. The DFD would make use of these potential benefits of the PFRC.

The features of the proposed DFD including its compactness and linear form, and that it will be limited to 1 to about 10 MW, make the DFD well-suited to a variety of space missions.

4.2. PFRC-2 experimental results

ARPA-E funding was provided to upgrade the PFRC-2, required for entry into the theoretically predicted ion heating regime. [30]. These

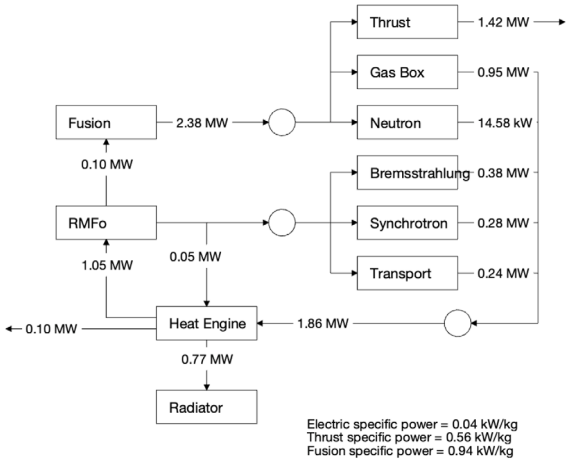

Fig. 9. Power model for the transfer vehicle engine.

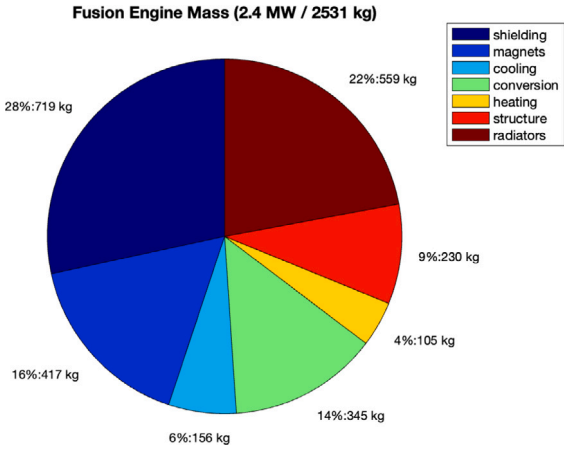

Fig. 10. Mass Breakdown for the transfer vehicle engine.

upgrades involve the implementation of four co-axial coils to increase magnetic field and modification of RF amplifiers, transmission lines, and tank circuits to decrease RMF frequency.

The target operating parameters are 0.1 T central magnetic field, 200 kW forward RF power, and an operating frequency below 2 MHz. The PFRC-2 has been operating at 1.8 MHz since November, 2022 and field upgrades are underway. Separately, ARPA-E funded construction of a stripping-cell electrostatic ion-energy analyzer (SC-IEA) [31,32] which will be utilized in 2023. Its energy range is 200 to 2000 eV with a resolution of $\Delta E/E \sim 7\%$.

New publications over the past year include measurements of neutral density in PFRC-2 using a two-photon-absorption laser-induced fluorescence (TALIF) diagnostic [33], the improvement of X-ray data analysis for electron temperature measurements [34,35], a rigorous proof of magnetic-field-line closure using modified flux functions [36], and the construction of a collisional-radiative model for bulk electron temperature measurements in warm hydrogen plasma [37]. The TALIF diagnostic achieved temporal and spatial resolutions of 10 μs and 1 mm respectively, and a minimum detectable density less than 10^{10} cm^{-3}. Knowledge of the neutral density is critical to assessing and controlling plasma current loss and particle and energy confinement in present-day fusion reactor devices.

The path to transition from PFRC-2 to a pilot plant reactor PFRC involves the construction and testing of the next iteration, PFRC-3, a device with ten times stronger field (~1 T) using a low-temperature superconductors, operating with a larger plasma radius (16 cm), higher density (~10^{14}/cc) with a goal of reaching fusion-relevant temperatures (~10 keV temperatures). This would be followed by PFRC-4, which would function as a prototype reactor power plant using D-^{3}He (~100 keV ion temperature goal) and would test the complete power conversion system. Further details on the proposed path from PFRC-2 to a reactor PFRC can be found in Ref. [25].

4.3. Reactor power and mass breakdowns

The following figures show the engine designs, power flow, and mass breakdowns for the transfer vehicle and aircraft engines. The transfer vehicle engine power flow is shown in Fig. 9.

Fig. 10 shows a mass breakdown of the transfer vehicle engine. The specific mass computation includes not only the magnets and their cooling equipment, structure, heating, and conversion subsystems, but also the shielding and radiators. The heating and conversion systems are scaled from simple specific mass factors. The mass is dominated by the radiators. 100 kW is available for electric power use in spacecraft.

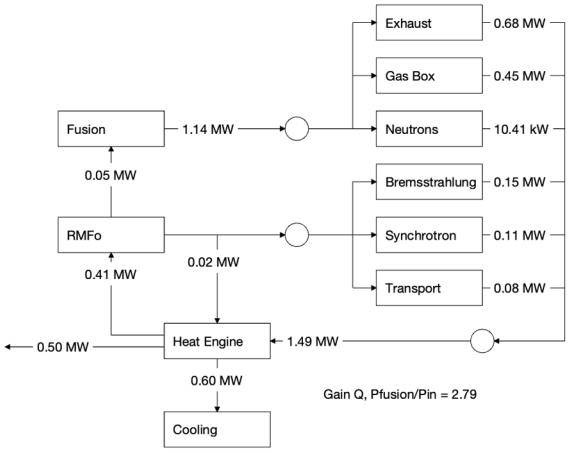

Fig. 11. Power model for the aircraft engine.

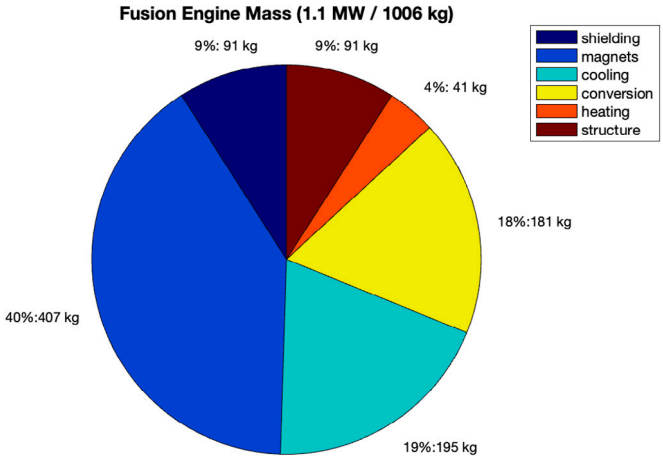

Fig. 12. Mass Breakdown for the aircraft engine.

The magnet subsystem includes an array of eight flux-conserving, superconducting magnets and two stronger mirror magnets. The magnet cryocoolers are a substantial additional mass. The axial magnets will maintain a central field of 5.3 T while the mirror magnets will require a field of about 15 to 20 T.

Fig. 11 shows the power flow for the aircraft engine. Fig. 12 shows the mass breakdown.

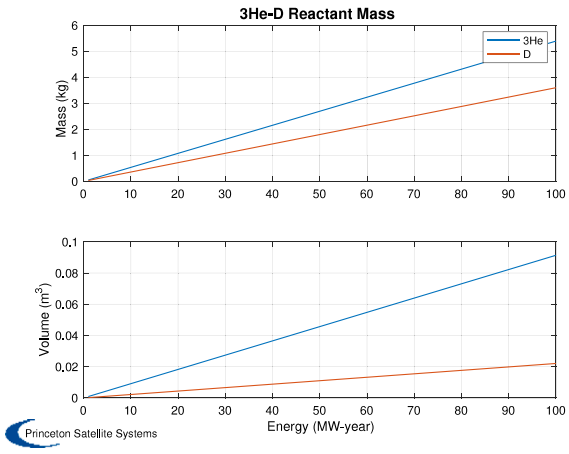

Fig. 13. The consumption of helium-3 fusion fuel as a function of time and power.

Fig. 14. Transfer vehicle.

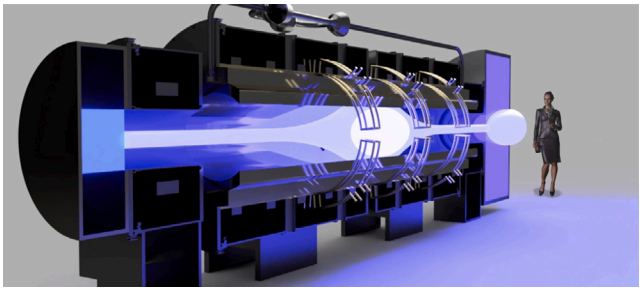

Fig. 15. 1 MWe power reactor similar to one proposed for the Titan aircraft.

Fig. 13 shows the consumption of helium-3 fusion fuel as a function of time and power. The mass of helium-3 is small. Additional propellant flows around the fusion region. This is expelled to produce thrust, or recirculated in a power reactor.

Fig. 14 shows the transfer vehicle.

4.4. DFD engine

Fig. 15 shows a CAD model of a reactor configured as a power reactor. This type of reactor would be used on the Titan aircraft.

A reactor configured as a rocket engine is shown in Fig. 16. A magnetic nozzle is on the end. The cutaway view does not show the heat engine.

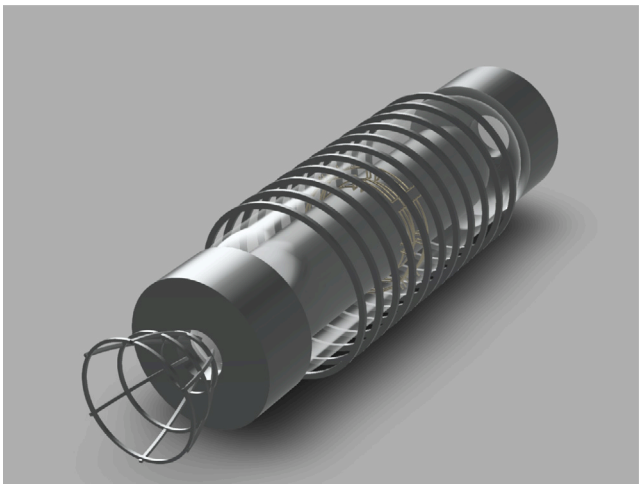

Fig. 16. 1 MWe power reactor configured as a rocket engine.

Table 7
Mission requirements for the titan aircraft.

Requirement	Value
Cruise speed	100 m/s
Takeoff distance	500 m
Cruise altitude	1 km

5. Titan aircraft design

In this section, the Titan Aircraft sizing and performance analysis in NASA's OpenVSP is presented.

5.1. Mission requirements

The design of the Titan Aircraft was driven by the key mission requirements. The mission requirements for the aircraft are presented in Table 7.

In addition to these mission requirements, certain assumptions about the aircraft were made. The assumption was made that there is constant electric power of up to 1MW coming from the fusion reactor during all stages of subsonic flight once in Titan's atmosphere. Another key assumption was that the aircraft never loses any mass due to fuel burn. This means there was no need for any initial weight fraction calculations since it was assumed the dry mass of the aircraft will be 2000 kg for all stages of flight. The mass of the engine was assumed to be a constant 1000 kg.

One of the major mission requirements is the fact that it is a hypersonic reentry vehicle, and therefore it has to take into account aerodynamic heating effects [38]. The aerodynamic heating that dominates hypersonic flows is typically thermal conduction and radiation. Thermal conduction takes place when a temperature gradient exists, and the heat transfer to the surface q_w is given by Fourier's law [38]:

$$q_w = -k_w\left(\frac{\partial T}{\partial y}\right)_w \tag{5}$$

where k_w is the thermal conductivity of the gas at the wall, and $\left(\frac{\partial T}{\partial y}\right)_w$ is the temperature gradient in the gas at the wall [38]. Thermal radiation will only occur if the flowfield around the body is over approximately 10,000 K. If the gas temperature is high enough, viscous dissipation can occur [38]. Additionally, a chemically reacting boundary layer can form, and the vibrational energy of the molecules can become excited to the point where dissociation and even ionization of the gas occur [38]. For hypersonic entry vehicles such as this, radiative effects and potential ionization within the gas are important [38]. While the study of the aircraft's performance at the cruise Mach number does not

account for the aerodynamic heating felt by hypersonic entry vehicles, all hypersonic vehicles have blunt noses to alleviate the aerodynamic heating on the body [38]. Therefore, this vehicle is shown to have a blunt nose.

Before any sketching of the aircraft could occur, initial conceptual sizing was necessary to make sure a design that met all of the mission requirements was feasible. As stated above, there was no need to go through calculations for a takeoff weight buildup or estimate fuel fractions for different stages of flight, since the aircraft weight would always remain constant at 2000 kg due to the fusion reactor's constant electric power source. Therefore, the take-off weight calculation was unnecessary, and it was possible to go right to airfoil and geometry selections.

5.2. Wing loading and geometry selection

The airfoil selection is incredibly important to the lift and drag of the aircraft. For the initial design, a NACA 0010 airfoil was chosen, but a symmetric double-wedge shape was chosen for the final design since the aircraft will be subjected to hypersonic flow when entering Titan's atmosphere.

After choosing an initial airfoil for the wing, the power-to-weight ratio and wing loading needed to be calculated. The power-to-weight ratio is used to describe a propeller-powered aircraft and is the equivalent to the "thrust-to-weight" term for a jet engine aircraft [39]. Since this aircraft is driven by ducted fans when in subsonic, compressible flow in Titan's atmosphere, the power-to-weight ratio is needed. A critical parameter in wing loading is the stall speed. The stall speed of the aircraft is directly determined by the wing loading and the maximum lift coefficient and is critical to flight safety [39]. The approach speed, which is also used to determine takeoff length, is defined by the stall speed [39]. The FAA defines acceptable stall speeds for different types of aircraft based on applications [40]. Since the coefficient of gravity on Titan is around 7.3 times weaker than on Earth, the stall speed is going to be much lower for an aircraft on Titan. Given the gravity constant on Titan is

$$1.352\ \mathrm{m/s^2} \tag{6}$$

In the following equations, TO refers to takeoff. As well as the required takeoff field length of 500 m, kinematic equations were used to estimate the stall speed [39]:

$$s_{TO} = \frac{1}{2}at^2 \tag{7}$$

$$t = \sqrt{\frac{2s_{TO}}{a}} \tag{8}$$

$$v_{final} = v_{initial} + at \tag{9}$$

$$= v_{TO} \tag{10}$$

The stall velocity is dependent upon the takeoff speed and is given through the following formula [39]:

$$v_{stall} = \frac{v_{TO}}{1.2} \tag{11}$$

The stall speed adds a vertical line to the thrust loading vs wing loading graph and acts as the maximum limit for W/S. The design must be to the left of this vertical line. Given this estimate of stall speed, the wing loading could be estimated. The wing loading is given by the following equation [39]:

$$V_{stall} = \sqrt{\frac{W}{S}\frac{\rho}{C_{l_{max}}}} \tag{12}$$

($C_{l_{max}}$) was estimated as 3.0 for STOL aircraft.

Given the above parameters, the maximum wing loading was found with the following formula [39]:

$$\frac{W}{S} = \sqrt{\frac{V_{stall}C_{l_{max}}}{\rho}} \tag{13}$$

This is the vertical line on the thrust-to-weight vs. wing loading graph, which provides a design constraint for the aircraft.

The thrust-to-weight and power-to-weight vs. wing loading feasibility diagram for different stages of the flight was then generated in MATLAB, which provides key design points from which the aircraft may be sketched. The constant weight of the aircraft will drastically impact the power-to-weight vs. wing loading graph and the design point is chosen. All equations from this graph come from the master equation [41]:

$$\frac{T_{s.l.}}{W_{TO}} = \frac{\beta}{\alpha}\left(\frac{q_{\inf}S}{\beta W_{TO}}\left(K_1\left(\frac{n\beta W_{TO}}{q_{\inf}S}\right)^2 + K_2\left(\frac{n\beta W_{TO}}{q_{\inf}S}\right) + C_{D_0} + C_{D_R}\right) + \frac{P_s}{V}\right) \tag{14}$$

First, the thrust-to-weight ratios were found. The thrust-to-weight ratio at cruise represents the amount of thrust needed to maintain the cruise velocity of 100 m/s. The equation for thrust loading during cruise is given by the following equation [42]:

$$\frac{T_{sl}}{W_{TO}} = \frac{\beta}{\alpha}\left(\frac{k\beta}{q}\frac{W_{TO}}{S} + \frac{C_{d_0}}{(W_{TO}/S)\left(\frac{\beta}{q}\right)}\right) \tag{15}$$

The thrust-to-weight ratio during takeoff is dependent on the thrust-to-weight ratio during cruise [39]:

$$\frac{T_{TO}}{W_{TO}} = \frac{T_{cruise}}{W_{TO}}\frac{W_{cruise}}{W_{TO}}\frac{T_{TO}}{T_{cruise}} = \frac{T_{cruise}}{W_{TO}}\frac{T_{TO}}{T_{cruise}} \tag{16}$$

Finally, the thrust-to-weight ratio during climb is given by [39]:

$$\frac{T_{climb}}{W_{TO}} = \frac{q_{climb}C_{d_0}}{W/S} + k\left(\frac{W}{S}\frac{n}{q_{climb}\pi A\epsilon}\right) \tag{17}$$

The relation between the thrust-to-weight ratio and the power-to-weight ratio is given by the following equation [39]:

$$\frac{T}{W} = \frac{500\ \eta_{prop}}{V}\frac{hp}{W} \tag{18}$$

where η_{prop} is the efficiency of the propellers, calculated in the next section, and hp is the horsepower of the aircraft. The thrust-to-weight ratios were calculated for the takeoff, climb, and cruise segments and then were converted to power-to-weight terms using the above equation before being plotted in MATLAB as functions of wing loading for different values of wing loading, varying from 1 to 50.

The final horsepower-to-weight vs. wing loading graph is shown below in Fig. 17. The horsepower-to-weight ratio is a reworked version of the traditional thrust-to-weight ratio specifically for propeller driven aircraft.

The final thrust-to-weight curve is shown below in Fig. 18.

These two curves allow for the selection of a design point for the aircraft. Since the wing loading for stall is at 27.0849, the design must be to the right of this curve. The design point must also be above the cruise and climb curves on the graph and to the left of the maximum allowable wingloading. The climb is the lowest curve, so the design point must be above that curve. A wing loading value of 25 was chosen. From this W/S value, the initial wing geometry was calculated, beginning with the wing area (s):

$$\frac{W}{s} \tag{19}$$

The wing area, s, was found to be 108.16 $\mathrm{m^2}$. Next, the wing span can be found given the formula [39]:

$$b = \sqrt{As} \tag{20}$$

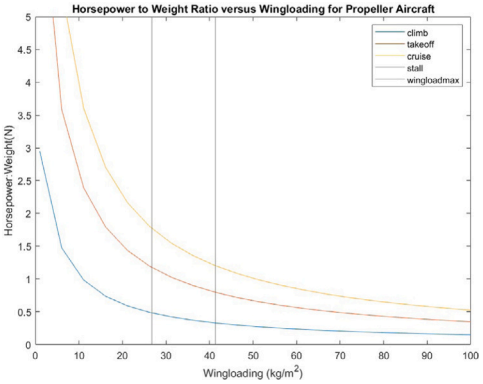

Fig. 17. Horsepower-to-Weight vs. Wing Loading MATLAB Plot.

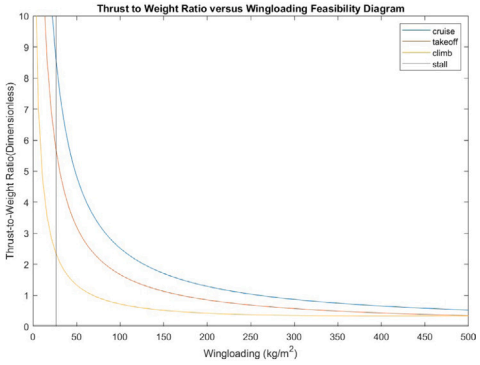

Fig. 18. Thrust-to-Weight vs. Wing Loading MATLAB Plot.

where A refers to the aspect ratio, estimated from the initial engine data to be 1.7. Next, the root chord was estimated through the following formula [39]:

$$C_{root} = \frac{2S}{b(1+\lambda)} \tag{21}$$

where λ is the taper ratio, the ratio between the tip chord and the center line root chord. Since the wing will be a delta wing and will have a high sweep, the taper ratio is estimated for now to be 0.25. The tip chord is simply the product of the taper ratio and the root chord [39]:

$$C_{tip} = \lambda C_{root} \tag{22}$$

The mean aerodynamic chord can be estimated as [39]:

$$C_{mean} = \frac{2}{3} C_{root} \frac{1+\lambda+(\lambda)^2}{1+\lambda} \tag{23}$$

Finally, the span-wise mean aerodynamic chord's location from the center line for a wing or a tail is given by [39]:

$$Y_{bar} = \frac{b}{6} \frac{1+2\lambda}{1+\lambda} \tag{24}$$

5.3. OpenVSP sketching and analysis

After setting initial parameters for the main wing geometry, the first iteration of the aircraft was sketched in NASA's Open Vehicle Sketch Pad. A NACA 0010 airfoil was used, with the intention that multiple airfoil configurations would be tested.

A delta-wing has six ducted fan engines placed near the back of the fuselage to take advantage of Boundary Layer Ingestion. These are covered during entry. Boundary-Layer Ingestion involves the placement of electric propulsors like ducted fans, rotors, or propellers so that they ingest the fuselage boundary layer flow near the tail end of the fuselage [43]. Boundary-Layer Ingestion systems increase propulsive

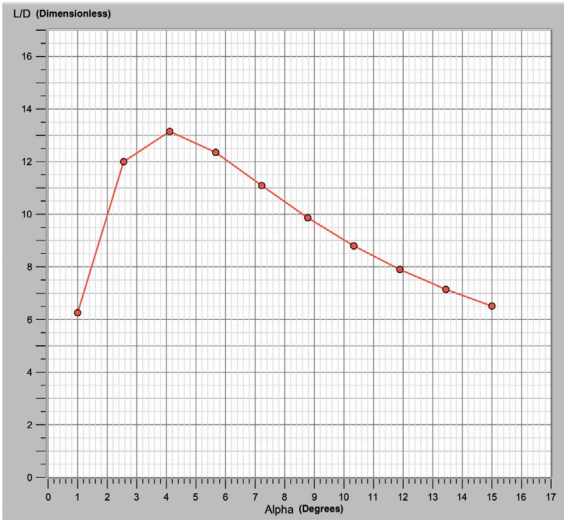

Fig. 19. L/D vs. Angle of attack for the initial aircraft design.

efficiency by reducing drag and can be implemented on the hybrid wing body [43], which is the configuration of this aircraft. The ducted fans are both connected in parallel to the fusion reactor main engine, so it is assumed that there is constant power across both of them. The ducted fans are modeled as actuator disks in OpenVSP. A simple vertical stabilizer with a NACA 0010 airfoil was chosen for the initial aircraft. This configuration was then analyzed using the VSPAero vortex lattice solver, with the Karman-Tsien compressibility correction to account for the subsonic compressible flow that occurs over the airfoil at the cruise Mach of 0.75. L/D was analyzed for varying angles of attack from 1–15. The analysis results are shown in Fig. 19.

At an angle of attack of 3, the L/D ratio is a little over 13, which is much less than the assumed L/D in the thrust-to-weight vs. wing loading MATLAB code (L/D at cruise was assumed to be 18). The initial airfoil chosen was ultimately changed to the double-wedged airfoil, due to its common use in supersonic and hypersonic applications. As this is meant to be a hypersonic entry vehicle, the aircraft will need to have an airfoil that can handle flow conditions beyond subsonic flight. Hypersonic flow is defined as the regime where certain physical flow phenomena become more important as the Mach number increases. These phenomena are as follows: thin shock layers, strong entropy gradients in the nose that cause vorticity interaction, viscous dissipation, a chemically reacting boundary layer, low-density flow, and high-temperature effects [38]. Using one of three surface inclination methods: Newtonian theory, the tangent wedge approximation, or the shock-expansion method, one can approximately solve for the pressure gradients and forces over the airfoil in the hypersonic flow regime [38]. Wedged airfoils have sharp leading edges to reduce wave drag, and the aerodynamic performance can be analyzed via the Newtonian method, tangent wedge method, or shock-expansion method [44].

Wave drag in supersonic flight is caused by the formation of normal shock waves in supersonic flow that detach from the leading edge of the wing [44]. When inserted into a freestream hypersonic flow, a wedge experiences an attached oblique shock at the nose, followed by the formation of expansion waves around the corner of the wedge, and another oblique shock at the back of the wedge [38]. This is compared to a blunt body, which experiences a bow shock at the nose, with the potential to detach from the body [38]. Having a blunt leading-edge airfoil increases this drag, but having a sharp leading-edge airfoil allows the oblique shock waves described above to attach to the leading edge and decreases the area of high pressure ahead of the wing, therefore reducing wave drag [44].

Other changes were implemented for the final iteration. First, distributed electric propulsion was utilized for its many benefits, to be

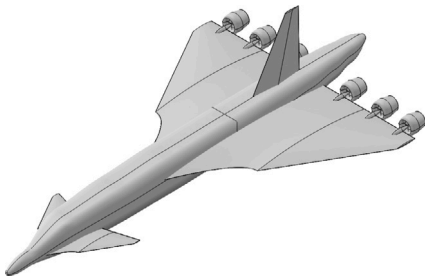

Fig. 20. Final iteration of the Titan aircraft, with a delta wing, six propellers, and a canard.

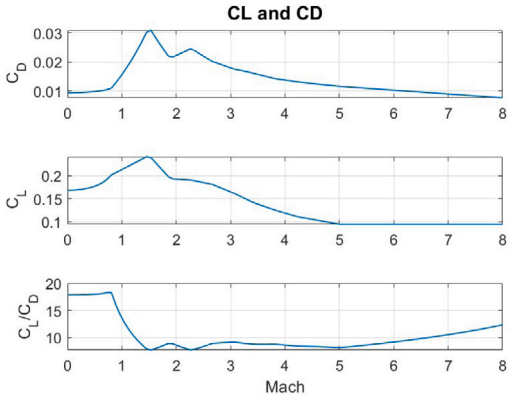

Fig. 21. C_l, C_d, and C_l/C_d versus Mach Number for the Final Titan Aircraft Design.

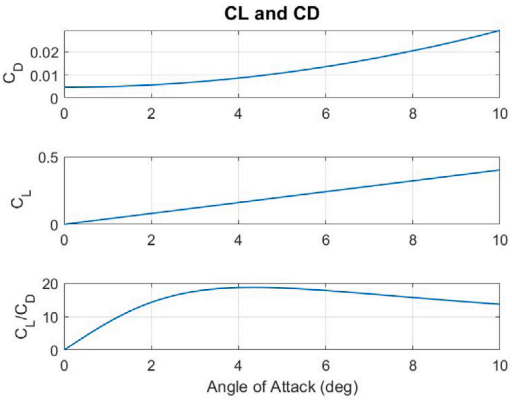

Fig. 22. C_l, C_d, and C_l/C_d versus Angle of Attack for the Final Titan Aircraft Design.

described below. Six ducted fans which were shrouded during hypersonic entry were added to the aircraft. A canard was also added for increased lift and stability in the subsonic regime. It would be retracted during the hypersonic entry. Finally, as mentioned, a double-wedged airfoil was utilized in the final iteration. The final Titan aircraft is shown in Fig. 20.

5.4. Tail configuration and sizing

Since delta-winged aircraft do not need horizontal stabilizers, it was decided that only a vertical tail (vertical stabilizer) was necessary. Every iteration utilized a delta wing in some way, so none of the designs have horizontal stabilizers. The tail is sized via the vertical tail volume coefficient C_{VT}, and its equation is shown below [1]:

$$C_{VT} = \frac{L_{VT} S_{VT}}{b_w S_w} \tag{25}$$

where L_{VT} is the moment arm of the vertical tail and is approximated as the distance from the tail quarter chord to the wing quarter-chord and S_{VT} is the area of the vertical tail [1]. Other delta-winged aircraft with vertical tails were investigated and used to estimate the vertical tail volume coefficient. C_{VT} was found to be 0.07. Since b_w and S_w were found in the wing loading section, the tail area, S_{VT}, can be solved for.

5.5. Flight envelope

For the final model, graphs of C_l, C_d, and C_l/C_d versus Mach number were graphed in VSPAero and MATLAB in order to demonstrate performance. The Mach number demonstrates compressibility effects on the airflow [45]. Shock waves will be present above Mach 1 during hypersonic re-entry, so it is important to make sure the aircraft can still generate enough lift. The aircraft's performance over the entire flight envelope must be evaluated, to make sure it can operate during the various stages of flight: hypersonic entry, cruise, descent, landing, and takeoff. The performance is measured through the aircraft's C_l and C_d values over the flight envelope. The critical performance graph for the final design is shown in Fig. 21.

Additionally, graphs of C_l, C_d, and C_l/C_d versus angle of attack were constructed to show how the aircraft responds to different pressure differentials between windward and leeward surfaces. The second critical performance graph is shown in Fig. 22.

According to these graphs, the maximum value of C_l/C_d is 18.74, occurring at an angle of attack of 4.44°. This is more than the initial estimate of L/D in the thrust to wing loading graph during cruise, which was 18.

5.6. Distributed electric propulsion

Ducted fans were chosen over propellers since the duct enclosing the mechanical fan reduces thrust losses due to propeller tip speeds and increases the efficiency of the propeller [46]. Six distributed fans were chosen due to the many advantages of distributed electric propulsion systems. Distributed electric propulsion is a type of propulsion system where multiple electrically-driven propellers are connected to energy sources or power-generating devices [47]. Distributed electric propulsion offers the opportunity for more efficient propulsion and overall improved aircraft performance due to its many aero-propulsive coupling effects [47]. First, distributed electric propulsion can increase the boundary layer ingestion benefits described earlier in this chapter for improved propulsive efficiency [47]. Boundary layer ingestion can also lead to wake filling. Wake filling is used to help reduce energy losses from friction in the aircraft's trailing wake [48]. Additionally, the placement of the ducted fans can be used to mitigate the trailing vortices for increased lift [47].

5.7. Sizing

The six ducted fans were sized as distributed propellers, therefore the speed-power coefficient was first calculated to size the fan. The speed-power coefficient is defined by the equation:

$$C_s = V_{cruise} \left(\frac{\rho}{P n^2} \right)^{1/5} \tag{26}$$

where n is the rotation speed of the fan and P is the power coming into the fan. The power coming into the fan is from the fusion engine, and each of the fans is connected in parallel to the main power source. Given the fusion power reactor can output up to 1 MW of total power, each fan theoretically has up to 166 kW of power available to it. However, it was determined that only 28 kW of power was needed to drive each fan during cruise to maintain desired velocity. A rotation speed of 4000 RPM was estimated, based on similar engine data. Given these parameters, the speed power coefficient was found to be 2.0097.

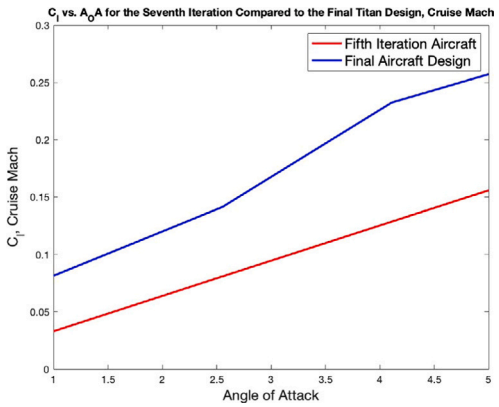

Fig. 23. C_l versus Angle of Attack Comparison between the Fifth Iteration and Final Design.

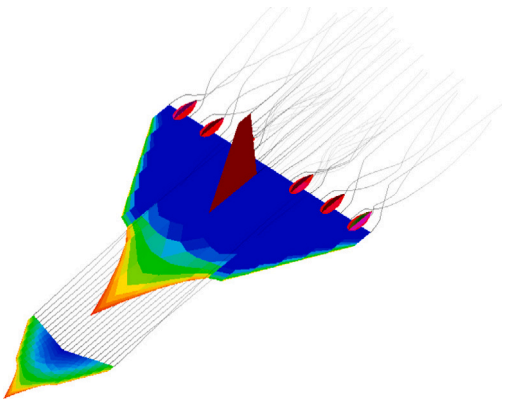

Fig. 24. Trailing Wakes and Vorticity for the Final Design at Angle of Attack of 4.11°.

With the speed power coefficient, key parameters for each fan can be found using the NACA 640 charts, such as the advance ratio (J), fan efficiency, and the pitch of the fan. The NACA 640 Chart was used to estimate each fan as a propeller with a Clark Y airfoil and three blades, the chart used to find the advance ratio, efficiency, and pitch. The advance ratio was found to be 0.8, therefore the blade angle at 0.75 R, also known as the pitch, is 15°. The efficiency of the fans is 0.82. The diameter of each fan is found with the formula:

$$D = \frac{V_{cruise}}{nJ} \tag{27}$$

From this formula, the diameter of each propeller is around 5 ft.

After finding the diameter, the coefficient of power and coefficient of thrust can be determined. The coefficient of power for the fan is found with the formula [1]:

$$C_p = \frac{P}{\rho n^3 D^5} \tag{28}$$

C_p was found to be 0.004.

The coefficient of thrust is found with the formula [1]:

$$C_T = \frac{\eta C_p}{J} \tag{29}$$

The coefficient of thrust was found to be 0.996.

Finally, the thrust needed for each fan is found through the formula

$$T = A_{fan} N_{fans} C_T \tag{30}$$

where A_{fan} is the area of each fan, and N_{fans} is the total number of fans. The thrust is 117.4 N.

5.8. Trailing wakes and optimal number of fans

To determine the optimal number of ducted fans, the lift coefficient distribution needs to be analyzed for each DEP configuration. The ducted fans need to contribute to the aircraft's lift force, so the number of fans that provide the best lift for the aircraft without trailing wake interference will be the optimal number of fans. The C_l versus angle of attack graph for the final aircraft design was generated in the above section. Comparing it to the fifth iteration of the aircraft, which has four distributed fans, yields the plot in Fig. 23.

This graph shows that during the transonic cruise, the six ducted fan configuration produces slightly more lift than the four ducted fan configuration, over a range of AOA from 0–10°. Therefore, the six-fan design is the better choice. The trailing wakes also need to be investigated when working with distributed propulsion. The trailing wakes for the final design are shown in Fig. 24.

As seen in Fig. 15, strong vortices are forming over the wing, which will lead to increased lift during landing and takeoff [45].

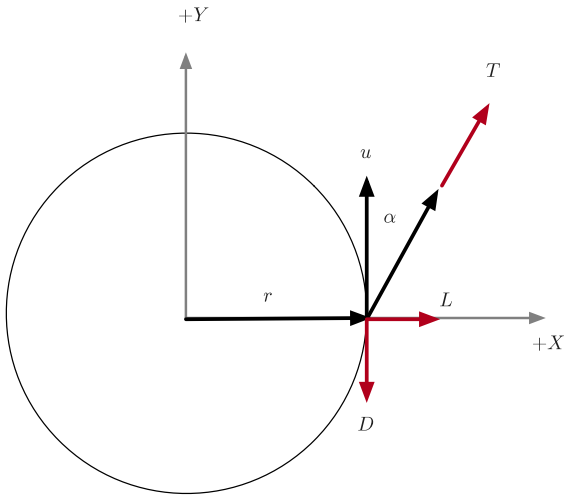

Fig. 25. Radial coordinates showing drag, lift, and thrust. u is the unit velocity vector.

Table 8
Aircraft parameters.

Parameter	Symbol	Value
Mass	m	2000 kg
Wing span	b	13.56 m
Root chord	C_{root}	12.8 m
Wing area	s	108 m^2
Vertical tail area	S_{VT}	11.34 m^2
Aspect ratio	A	1.9
Number of engines		6 ducted fan
Power per engine		160 kW
Takeoff distance	$s_{takeoff}$	500 m

6. Aircraft optimal entry and landing

A two-dimensional model was used for atmospheric entry. The vehicle parameters are given in Table 8.

The dynamical equations are the point mass polar equations of motion. The coordinates are shown in Fig. 25.

The equations of motion are:

$$\dot{v}_r = \frac{v_t^2}{r} - \frac{\mu}{r^2} + a_r \tag{31}$$

$$\dot{v}_t = -\frac{v_t v_r}{r} + a_t \tag{32}$$

$$\dot{r} = v_r \tag{33}$$

$$a = \frac{T + D + L}{m} \tag{34}$$

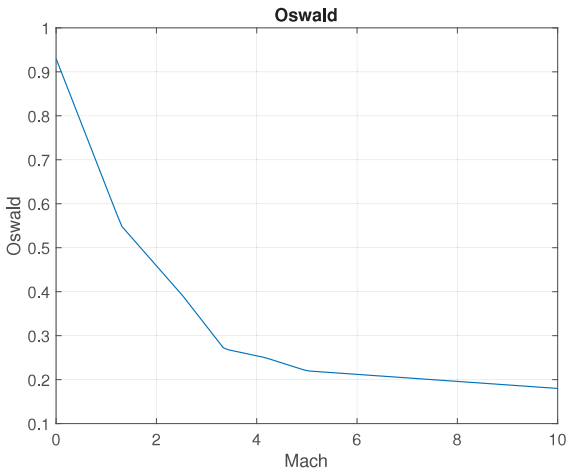

Fig. 26. Oswald efficiency factor for the range of Mach numbers in the optimal landing.

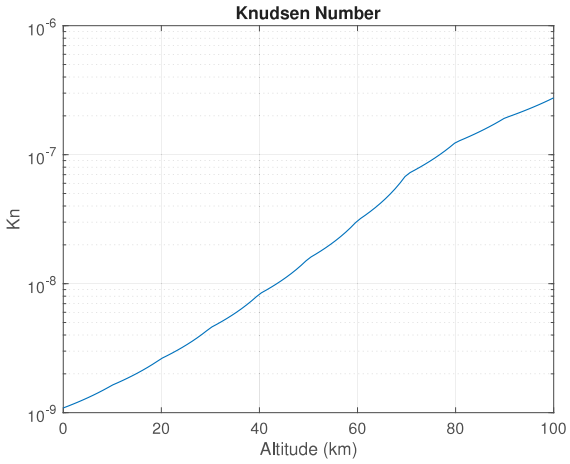

Fig. 27. Knudsen number, $\epsilon(M)$, for Titan.

$$q = \frac{1}{2}\rho(v_r^2 + v_t^2) \tag{35}$$

$$u = \frac{\begin{bmatrix} v_r \\ v_t \end{bmatrix}}{\sqrt{v_r^2 + v_t^2}} \tag{36}$$

$$D = -c_d q s u \tag{37}$$

$$L = c_l q s \begin{bmatrix} 0 & 1 \\ -1 & 0 \end{bmatrix} u \tag{38}$$

$$c_l = c_{l_\alpha}\alpha \tag{39}$$

$$c_d = c_{d_0} + \frac{c_l^2}{\pi A \epsilon(M)} \tag{40}$$

u is the velocity unit vector, T is thrust, and s is the aerodynamic surface area. The Oswald efficiency factor, $\epsilon(M)$ is a function of M and is shown in Fig. 26. The downrange state is not included. v_r is radial velocity and v_t is the tangential velocity. The thrust vector is aligned with u when $\alpha = 0$. The thrust vector is

$$T = \begin{bmatrix} \cos\alpha & -\sin\alpha \\ \sin\alpha & \cos\alpha \end{bmatrix} u \tag{41}$$

The continuum flow approximation is valid for the entire range of altitudes and velocities as shown in Fig. 27.

The landing is shown in Fig. 28. The optimization uses the MATLAB function `fmincon`. The cost is the heating rate and the constraint is to reach the Titan surface with zero velocity. Thrust is only required at the very end.

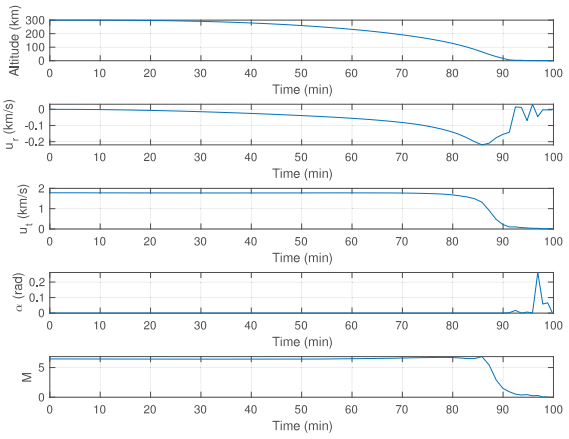

Fig. 28. Optimal landing. Thrust is only needed at the very end. This assumes a touchdown.

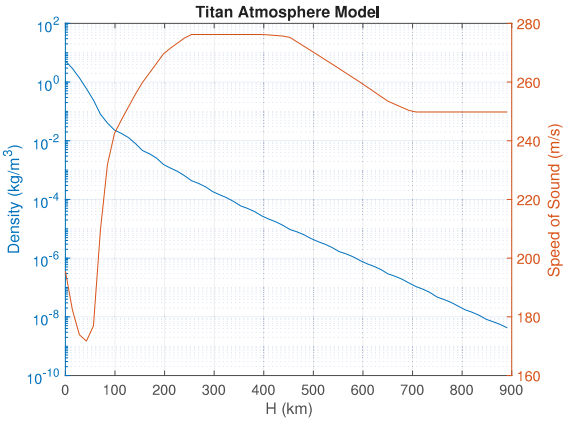

Fig. 29. Titan atmosphere model.

The atmosphere model is shown in Fig. 29. Titan's atmosphere is 98% nitrogen.

7. Conclusions

A nuclear fusion-powered transfer vehicle and aircraft could open new avenues for Titan scientific exploration. The paper presents a conceptual design-level analysis for both the orbiter and the aircraft. The short transit time to Titan means that Titan science work would start sooner. The high power in both the orbiter and aircraft would allow for new types of science that cannot be done with the power available on current robotic spacecraft. The work on the DFD is in the early experimental stage. The next machine, PFRC-3, will advance the technology in its 5-year life, to the point where planning for space propulsion can realistically begin. It is expected that the full development of a fusion propulsion system would take 10–15 years. It is potentially less expensive than nuclear electric fission because nuclear materials do not have to be handled. Small fusion has a potential terrestrial market so NASA would not need to bear the full development cost.

Declaration of competing interest

The authors declare that they have no known competing financial interests or personal relationships that could have appeared to influence the work reported in this paper.

Acknowledgments

Previous work on Direct Fusion Drive for interplanetary missions was supported in part by a NASA Innovative Advanced Concepts (NIAC), United States Grant NNX16AK28G. NASA STTRs NNX17CM47P and NNX17CC74P supported work on the radio-frequency heating and superconducting coil subsystems. Princeton Field Reversed Configuration experimental work is being conducted under the ARPA-E OPEN 2018, United States Grant DE-AR0001099. Work on power electronics for fusion power plants is supported under the ARPA-E GAMOW, United States grant DE-AR0001372. Thanks also to Dr. Slava Turyshev of JPL and Greg Meholic of The Aerospace Corporation for information on high power instruments.

References

[1] M. Gajeri, P. Aime, R.Y. Kezerashvili, A Titan mission using the Direct Fusion Drive, Acta Astronaut. 180 (2021) 429–438.
[2] T. Talbert, Dragonfly's Journey to Titan, 2020, https://www.nasa.gov/dragonfly/dragonfly-overview/index.html.
[3] NASA, Titan, 2021, https://solarsystem.nasa.gov/moons/saturn-moons/titan/in-depth/.
[4] S. Simon, A. Bößwetter, T. Bagdonat, U. Motschmann, K.-H. Glassmeier, Plasma environment of Titan: a 3-D hybrid simulation study, Ann. Geophys. 24 (3) (2006) 1113–1135, URL https://angeo.copernicus.org/articles/24/1113/2006/.
[5] J.W. Barnes, et al., Science goals and objectives for the dragonfly Titan rotorcraft relocatable lander, Planet. Sci. J. 2 (4) (2021) 130.
[6] R.D. Lorenz, E.P. Turtle, J.W. Barnes, M.G. Trainer, D.S. Adams, K.E. Hibbard, C.Z. Sheldon, K. Zacny, P.N. Peplowski, D.J. Lawrence, M.A. Ravine, T.G. McGee, K.S. Sotzen, S.M. MacKenzie, J.W. Langelaan, S. Schmitz, L.S. Wolfarth, P.D. Bedini, Dragonfly: A rotorcraft lander concept for scientific exploration at titan, Johns Hopkins APL Tech. Digest 34 (3) (2018).
[7] NASA, Huygens, 2021, https://solarsystem.nasa.gov/missions/huygens/in-depth/.
[8] S. Oleson, J. Hartwig, G. Landis, J. Walsh, R. Lorenz, M. Paul, Titan Turtle: NIAC Phase II Design for a Submersible Vehicle for Titan Exploration, in: Transformative Technologies for Space Exploration I, 2020.
[9] Titan Saturn System Mission NASA/ESA Joint Summary Report, https://sci.esa.int/documents/34334/35976/1567257786526-TSSM_Joint-Summary-Report_Public-Version_090120.pdf.
[10] J.L. Green, B.W. Reinisch, P. Song, S.F. Fung, R.F. Benson, W.W.L. Taylor, J.F. Cooper, L. Garcia, T. Markus, D.L. Gallagher, P. Gogineni, Radio Sounding Science at High Powers, in: 55th International Astronautical Congress of the International Astronautical Federation, the International Academy of Astronautics, and the International Institute of Space Law, 2004.
[11] National Research Council, Priorities in Space Science Enabled By Nuclear Power and Propulsion, The National Academies Press, Washington, DC, 2006.
[12] J. Downey, Traveling Wave Tube (TVT) RF Power Combining Demonstration for use in the Jupiter Icy Moons Orbiter (JIMO), in: Research Symposium II, 2004.
[13] C. Hartman, Forum on Concepts and Approaches for Jupiter Icy Moons Orbiter Science Capabilities & Workshop Goals, 2003, https://www.lpi.usra.edu/meetings/jimo2003/hartman.pdf.
[14] M. Hart, Jupiter Icy Moon Orbiter High Capability Instrument Feasibility Study Executive Summary, Tech. Rep. TOR-2004(2172)-3231, The Aerospace Corporation, 2004.
[15] JPL, Prometheus Project Final Report, Tech. Rep. 982-R120461, Jet Propulsion Laboratory, 2005.
[16] J. Pitman, A. Duncan, D. Stubbs, R. Sigler, R. Kendrick, E. Smith, J. Mason, G. Delory, J. Lipps, M. Manga, J. Graham, I. Pater, S. Reiboldt, E. Bierhaus, J. Dalton, J. Fienup, J. Yu, Multiple Instrument Distributed Aperture Sensor (MIDAS) for remote sensing, Proc. SPIE - Int. Soc. Opt. Eng. 5570 (2004).
[17] Space Science Lab, U. Massachusetts, One Step Closer to Jupiter https://ulcar.uml.edu/pars.html,
[18] Y. Razin, M. Paluszek, E. Hamand, G. Pajer, J. Mueller, S. Cohen, A.H. Glasser, Compact aneutronic fusion engine, in: International Astronautical Congress, 2012.
[19] Y.S. Razin, G. Pajer, M. Breton, E. Ham, J. Mueller, M. Paluszek, A.H. Glasser, S.A. Cohen, A direct fusion drive for rocket propulsion, Acta Astronaut. 105 (1) (2014) 145–155.
[20] M. Paluszek, G. Pajer, Y. Razin, J. Slonaker, S. Cohen, R. Feder, K. Griffin, M. Walsh, Direct Fusion Drive for a Human Mars Orbital Mission, in: International Astronautical Congress, 2014, IAC-14, C4, 6.2.
[21] S.A. Cohen, M. Chu-Cheong, R. Feder, K. Griffin, M. Khodak, J. Klabacha, E. Meier, S. Newbury, M. Paluszek, T. Rognlien, S. Thomas, M. Walsh, Reducing neutron emission from small fusion rocket engines, in: IAC, 2015, IAC-15, C4.7-C3.5, 9, x28852.
[22] S.A. Cohen, R.D. Milroy, Maintaining the closed magnetic-field-line topology of a field-reversed configuration with the addition of static transverse magnetic fields, Phys. Plasmas 7 (6) (2000).
[23] S.A. Cohen, B. Berlinger, C. Brunkhorst, A. Brooks, N. Ferarro, D. Lundberg, A. Roach, A. Glasser, Formation of collisionless high-β plasmas by odd-parity rotating magnetic fields, Phys. Rev. Lett. 98 (2007) 145002.
[24] S.A. Cohen, C. Swanson, N. McGreivy, A. Raja, E. Evans, P. Jandovitz, M. Khodak, G. Pajer, T. Rognlien, S. Thomas, M. Paluszek, Direct fusion drive for interstellar exploration, J. Br. Interplanet. Soc. 72 (2) (2019) 38–50.
[25] C. Galea, S. Thomas, M. Paluszek, S. Cohen, The Princeton Field-Reversed Configuration for Compact Nuclear Fusion Power Plants, J. Fusion Energy 42 (4) (2023).
[26] M.A. Paluszek, E.M. Ham, Y. Razin, S.A. Cohen, In space startup method for nuclear fusion rocket engines, 2019, U.S. Patent 10, 229, 756.
[27] A. Ishida, H. Momota, L.C. Steinhauer, Variational formulation for a multifluid flowing plasma with application to the internal tilt mode of a field-reversed configuration, Phys. Fluids 31 (10) (1988) 3024–3034.
[28] E.S. Evans, S.A. Cohen, D.R. Welch, Particle-in-cell studies of fast-ion slowing-down rates in cool tenuous magnetized plasma, Phys. Plasmas 25 (042105) (2018).
[29] S.J. Thomas, M.A. Paluszek, S.A. Cohen, A. Glasser, Nuclear and Future Flight Propulsion - Modeling the Thrust of the Direct Fusion Drive, in: AIAA Joint Propulsion Conference, 2018.
[30] S. Cohen, C. Brunkhorst, A. Glasser, A. Landsman, D. Welch, RF plasma heating in the PFRC-2 device: Motivation, goals and methods, in: AIP Conference Proceedings, 2011.
[31] M.N. Notis, A.H. Glasser, S.A. Cohen, S. Abe, Electrostatic Energy Analyzer and Gas Stripping Cell to Measure Ion Temperature in the PFRC-2, in: 63rd Annual Meeting of the APS Division of Plasma Physics, American Physical Society, Pittsburgh, PA, 2021.
[32] M. Notis, Charge Exchange Ion Energy Analyzer for the PFRC-2 Plasma Device, Senior Thesis, Princeton University, 2022.
[33] A. Dogariu, S. Cohen, P. Jandovitz, E. Evans, S. Vinoth, C. Swanson, A diagnostic to measure neutral atom density in fusion-research plasmas, Rev. Sci. Instrum. (2022).
[34] C. Galea, C. Swanson, S. Cohen, S. Thomas, Use of a Mylar filter to eliminate vacuum ultraviolet pulse pileup in low-energy X-ray measurements, Rev. Sci. Instrum. 93 (093531) (2022).
[35] T. Ahsan, C.P.S. Swanson, C. Galea, S.P. Vinoth, T. Qian, T. Rubin, S.A. Cohen, Analysis and mitigation of pulse-pile-up artifacts in plasma pulse-height X-ray spectra, MDPI Plasma 6 (1) (2023) 58–71.
[36] T. Ahsan, S. Cohen, An analytical approach to evaluating magnetic-field closure and topological changes in FRC devices, Phys. Plasmas 29 (2022).
[37] S. Vinoth, E. Evans, C. Swanson, E. Palmerduca, S. Cohen, Evaluation of a collisional radiative model for electron temperature determination in hydrogen plasma, Rev. Sci. Instrum. 93 (093503) (2022).
[38] J.D. Anderson, Hypersonic and High Temperature Gas Dynamics, second ed., American Institute of Aeronautics and Astronautics, Inc., 2006.
[39] D.P. Raymer, Aircraft Design: A Conceptual Approach, in: AIAA education series, American Institute of Aeronautics and Astronautics, Washington, D.C, 1989.
[40] Airplane Flying Handbook Last Modified: 2020-02-28T11:50:46-0500 https://www.faa.gov/regulations_policies/handbooks_manuals/aviation/airplane_handbook/.
[41] Test(1).pdf: MAE332_S2021 Aircraft Design, 2019, URL https://princeton.instructure.com/courses/2559/files/435143?module_item_id=102800.
[42] J.D. Mattingly, W.H. Heiser, D.T. Pratt, Aircraft Engine Design, 2nd Edition, American Institute of Aeronautics and Astronautics, 2004.
[43] R. Jansen, D.M.L. Celestina, Electrical propulsive fuselage concept for transonic transport aircraft, in: International Society for Air Breathing Engines, 2019.
[44] Utah State University, Section 7, Lecture 2:Supersonic Flow on Finite Thickness Wings, URL http://mae-nas.eng.usu.edu/MAE_5420_Web/section7/section7.2.pdf MAE 5420 - Compressible Fluid Flow.
[45] R.F. Stengel, Flight Dynamics, Princeton University Press, 2004.
[46] R. Bontempo, M. Manna, Effects of Duct Cross Section Camber and Thickness on the Performance of Ducted Propulsion Systems for Aeronautical Applications, Int. J. Aerosp. Eng. 2016 (2016) e8913901, Publisher: Hindawi.
[47] H.D. Kim, A.T. Perry, P.J. Ansell, A Review of Distributed Electric Propulsion Concepts for Air Vehicle Technology, in: 2018 AIAA/IEEE Electric Aircraft Technologies Symposium, American Institute of Aeronautics and Astronautics, Cincinnati, Ohio, 2018.
[48] H.-J. Steiner, A. Seitz, Wieczorek, K. Plötner, A. Isikveren, M. Hornung, Multi-disciplinary Design and Feasibility Study of Distributed Propulsion Systems, in: 28th Congress of the International Council of the Aeronautical Sciences, vol. 1, ICAS, 2012.